

Predicted strong coupling of solid-state spins via a single magnon mode

Denis R. Candido,^{*,†} Gregory D. Fuchs,^{*,¶} Ezekiel Johnston-Halperin,^{*,§} and
Michael E. Flatté^{*,†}

[†]*Department of Physics and Astronomy, University of Iowa, Iowa City, Iowa 52242, USA*

[‡]*Pritzker School of Molecular Engineering, University of Chicago, Chicago, Illinois 60637,
USA*

[¶]*School of Applied and Engineering Physics, Cornell University, Ithaca, New York 14850,
USA*

[§]*Department of Physics, The Ohio State University, Columbus, Ohio 43210, USA*

^{||}*Department of Applied Physics, Eindhoven University of Technology, Eindhoven 5612 AZ,
The Netherlands*

E-mail: denisricardocandido@gmail.com; gdf9@cornell.edu; johnston-halperin.1@osu.edu;
michael_flatte@mailaps.org

Abstract

We propose an approach to realize a hybrid quantum system composed of a diamond nitrogen-vacancy (NV) center spin coupled to a magnon mode of the low-damping, low-moment organic ferrimagnet vanadium tetracyanoethylene. We derive an analytical expression for the spin-magnon cooperativity as a function of NV position under a micron-scale perpendicularly magnetized disk, and show that, surprisingly, the cooperativity will be higher using this magnetic material than in more conventional materials with larger magnetic moments, due to in part to the reduced demagnetization field. For reasonable experimental parameters, we predict that the spin-magnon-mode coupling strength is $g \sim 10$ kHz. For isotopically pure ^{12}C diamond we predict strong coupling of an NV spin to the unoccupied magnon mode, with cooperativity $\mathcal{C} = 6$ for a wide range of NV spin locations within the diamond, well within the spatial precision of NV center implantation. Thus our proposal describes a practical pathway for single-spin-state-to-single-magnon-occupancy transduction and for entangling NV centers over micron length scales.

Coherent spin centers in solids have emerged as an important solid-state quantum platform due to their applications to quantum sensing^{1,2} and quantum information^{3,4} as well as their potential for probes of fundamental quantum mechanical properties.⁵ In particular, negatively-charged nitrogen-vacancy (NV) spin centers in diamond^{6–8} are promising candidates for quantum memories and quantum networking^{9,10} due to their long-lived spin coherence combined with spin-selective optical properties. Creating and scaling entanglement between NV centers poses a key challenge because direct coupling between them is too weak for separations more than ~ 20 nm.^{11–13} Independent and simultaneous optical readout of two NV centers so closely positioned would require heroic efforts due to the spatial and emission-wavelength overlap of their fluorescence. An alternative scheme to couple two NV spins proposed the virtual exchange of magnons in ferromagnetic regions separated by a one-dimensional spin chain.¹⁴ Related work includes demonstrations of room-temperature coupling between NV centers and yttrium iron garnet (YIG) magnon modes in the classical

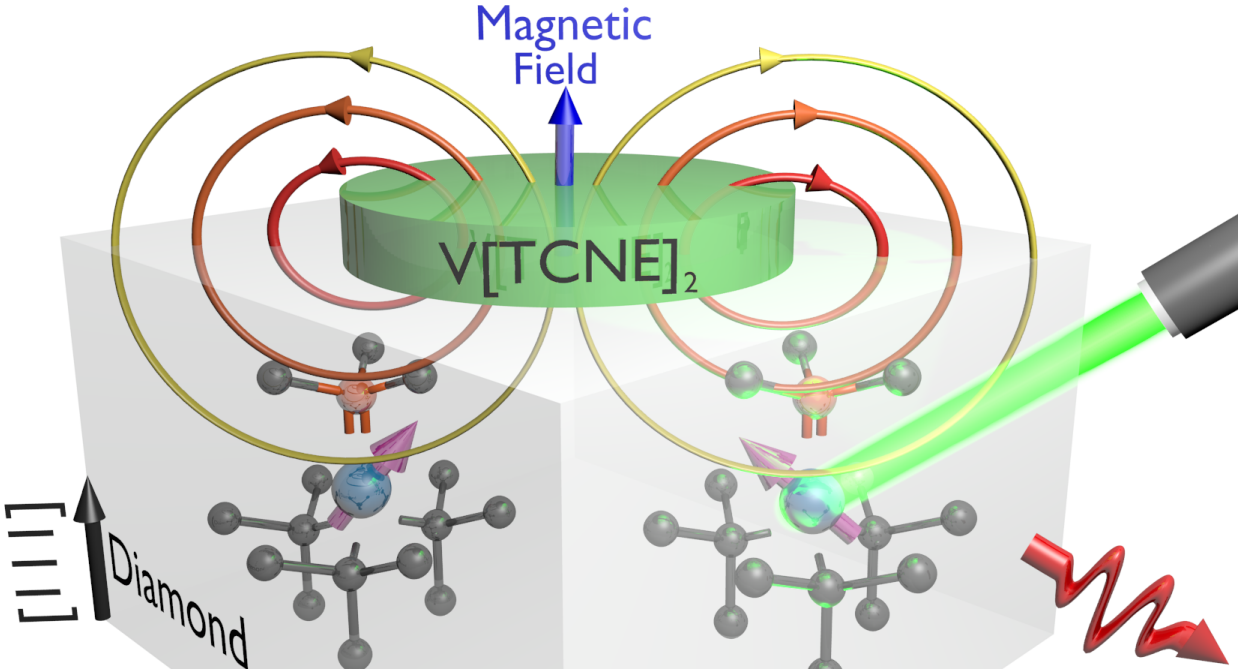


Figure 1: Schematic view of the strong quantum-coherent coupling between NV-center spin and magnon mode. The green disk represents the normally magnetized $V[TCNE]_x$ ferrimagnetic material placed on top of a diamond [111] substrate possessing NV centers.

regime.^{15–19} However, while YIG exhibits ultra-low magnetic dissipation, integrating this material with diamond poses significant hurdles. First, direct epitaxy on diamond has not been demonstrated, likely because of the substantial lattice mismatch. Second, YIG films exhibit a sizable increase in magnon damping both when they are patterned^{20,21} and at low temperature^{22,23} — both of which will be necessary to obtain strong interactions and low thermal magnon occupation. Recent efforts to address the first two points with a high temperature (800°C) post-growth annealing²⁴ show promise in restoring intrinsic material properties, but present their own challenges for device integration.

Here we propose a practical approach to engineer strong, coherent single-spin-single-magnon-mode (hereafter spin-magnon) coupling, which would permit transduction between the spin state of a single NV to the magnon occupancy of an otherwise unoccupied magnon mode. This hybrid quantum system can enable entanglement between NV centers separated by $\approx 1 \mu\text{m}$. Our proposal relies on the magnetic properties of the low loss organic ferrimagnetic material vanadium tetracyanoethylene^{25–32} ($V[TCNE]_x$) to overcome the challenges of

building and integrating low loss magnetic materials on diamond. $\text{V}[\text{TCNE}]_x$ can be grown without lattice-matched substrates and patterned at the micron scale into arbitrary shapes while maintaining its low magnetic damping³² (Gilbert parameter $\alpha = 4 \times 10^{-5}$, comparable to values obtained under the best conditions for YIG). Our proposal considers the resonant spin-magnon coupling (g) achievable at low temperature ($T \lesssim 100$ mK) with a micron-scale disk of perpendicularly-magnetized $\text{V}[\text{TCNE}]_x$ positioned on top of a single-crystal (111) diamond substrate with embedded NV centers (Fig. 1). Our analytical calculations predict $g \sim 10$ kHz between an NV spin 30 nm below the diamond surface and an unoccupied magnon mode of a micron-diameter, 100 nm thick disk. The strong in-plane fringe fields of the $\text{V}[\text{TCNE}]_x$ microstructure efficiently couple to an NV spin with axis perpendicular to the surface in a (111) diamond substrate.³³ Using an NV coherence time $T_2^* \approx 1.5 \times 10^{-3}$ s that is obtainable³⁴ in isotopically-pure ¹²C diamond, we obtain cooperativity $\mathcal{C} \approx 6$ for a range of NV center positions under the disk. This strong spin-magnon coupling, when combined with suitable gates to tune the system into and out of resonance, can be used to mediate controllable coupling between multiple NV centers separated from each other by microns but each coupled to the magnon mode. We further obtain an analytical formula for the spin-magnon cooperativity expressed as a product of the magnon frequency, a geometric, and a material factor. This allows us to compare the cooperativity for systems with different disk dimensions, as well as for different materials realized with the same geometry. Using this formula we predict a lower cooperativity for thin-film YIG compared to $\text{V}[\text{TCNE}]_x$, due to (1) the higher magnetic damping, and (2) the much higher resonance energy for a YIG magnon due to its much larger demagnetization field.

Magnons — The spin-magnon coupling g will be enhanced for high angular momentum magnon modes of a perpendicularly-magnetized disk ($\mathbf{B}_{dc} = \mu_0 \mathbf{H}_{dc} = B_{dc} \hat{z}$), which will localize the magnon mode near the edge of the disk. Analytic expressions for the magnon mode frequencies (ω), rf magnetization (\mathbf{m}) and fringe fields ($\bar{\mathbf{h}}$) for a disk of $\text{V}[\text{TCNE}]_x$

emerge from Maxwell's equations in the magnetostatic limit¹ together with the Landau-Lifshitz-Gilbert equation,

$$\nabla \times \mathbf{H} = 0, \quad (1)$$

$$\nabla \cdot \mathbf{B} = 0, \quad (2)$$

$$\frac{d\mathbf{M}}{dt} + \gamma \mathbf{M} \times \mathbf{H} = -\alpha(\gamma/M_S) \mathbf{M} \times (\mathbf{M} \times \mathbf{H}), \quad (3)$$

with the magnetic field $\mathbf{H} = (\mathbf{B}/\mu_0) - \mathbf{M}$. Here \mathbf{M} is the magnetization, μ_0 is the vacuum permeability, γ is the gyromagnetic ratio, α is the damping factor and M_S is the saturation magnetization (see Supplemental Material³⁵). The disk occupies the region $\mathcal{D} = \{(r, \theta, z), r < R \text{ \& } |z| < d/2\}$ and the substrate $\mathcal{S} = \{(r, \theta, z), z < -d/2\}$ (Fig. 1).

$$\omega_\lambda = \gamma \left\{ \tilde{H}_0^2 + \frac{\tilde{H}_0 M_S}{1 + (k_{i,l,m,n}^2/k_{0,m,n}^2)} \right\}^{1/2}, \quad (4)$$

where the mode index $\lambda = (m, n, l)$ stands for angular (m), radial (n) and thickness (l) modes. The analytical magnon frequencies obtained here [Eq. (4)] were experimentally and numerically validated for V[TCNE]_x disks.³² The fringe field $\mathbf{h}_\lambda(\mathbf{r}, t) = \text{Re} \{ \bar{\mathbf{h}}_\lambda(\mathbf{r}) e^{i\omega_\lambda t} \}$ within the \mathcal{S} region

$$\begin{aligned} \frac{\mathbf{h}_\lambda(\mathbf{r}, t)}{c_\lambda} = & \hat{r} \cos(m\theta + \omega_\lambda t) \frac{k_o}{2} [J_{m-1}(k_o r) - J_{m+1}(k_o r)] e^{k_o z} \\ & - \left[\frac{m\hat{\theta}}{r} \sin(m\theta + \omega_\lambda t) + \hat{z} k_o \cos(m\theta + \omega_\lambda t) \right] J_m(k_o r) e^{k_o z} \end{aligned} \quad (5)$$

with $k_o = \beta_{m-1}^n/R$, and $c_\lambda = (2\gamma\hbar M_S/k_{o,m,n}^2\kappa^2 I_{m,n}^r I_{l,m,n}^z)^{1/2}$ with $I_{m,n}^r = \int_0^R r dr J_{m-1}^2(k_{o,m,n} r)$ and $I_{l,m,n}^z = \int_{-\frac{d}{2}}^{\frac{d}{2}} dz Z^2(z)$.

¹As we are working with microwave frequencies ω and small magnetic samples, i.e., $R\omega/c \ll 1$, it follows $c|\mathbf{B}|/|\mathbf{E}| \gg (c/R\omega) \gg 1$, justifying the use of the magnetostatic version of Maxwell's equations.

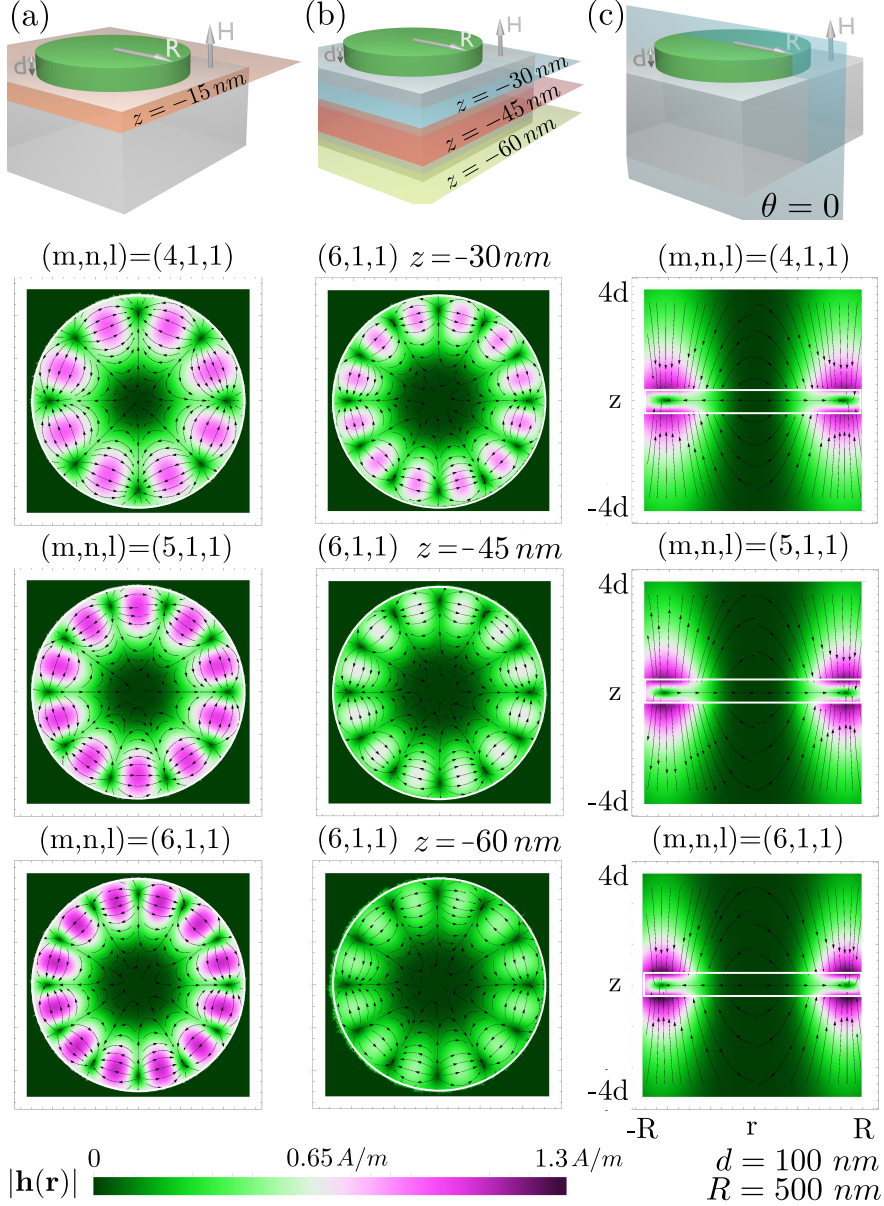


Figure 2: (a) In plane fringe fields $\mathbf{h}(\mathbf{r})$ at $z = -15$ nm (orange plane) for the modes $(4, 1, 1)$, $(5, 1, 1)$, $(6, 1, 1)$. (b) In plane fringe fields $\mathbf{h}(\mathbf{r})$ for the mode $(6, 1, 1)$ at depth $z = -30$ nm, $z = -45$ nm and $z = -60$ nm (blue, red and yellow planes, respectively). (c) Fringe fields $\mathbf{h}(\mathbf{r})$ for cross section view $\theta = 0$ (blue plane) for modes $(4, 1, 1)$, $(5, 1, 1)$, $(6, 1, 1)$. The white lines delimit the disk dimensions $R = 500$ nm and $d = 100$ nm.

Figure 2 presents the fringe field $\mathbf{h}_\lambda(\mathbf{r}, t)$ [Eq. (5)] for a $\text{V}[\text{TCNE}]_x$ disk with $d = 100$ nm, $R = 500$ nm, $M_S = 7560$ A/m,²⁶ $A_{ex} = 2.2 \times 10^{-15}$ J/m,³² $\gamma = (4\pi/1000) \times 2.73 \times 10^6$ Hz m/A,³² and $B = B_c \approx 56$ mT. The first column [Fig. 2(a)] displays the in plane $\mathbf{h}_\lambda(\mathbf{r}, t)$ profile for three different modes (m, n, l) at the interface $z = -15$ nm between the disk \mathcal{D}

and the diamond substrate \mathcal{S} [orange plane Fig. 2 (a)]. The largest fringe fields occur for the lowest thickness and radial modes² $l = 1$ and $n = 1$. The larger the magnon angular index m , the more localized the fringe field around the edge of the disk and the larger the amplitude of the fringe fields. Therefore, high angular index magnon modes are preferred for coupling to NV center spins.

The fringe field is largest near the interface between the magnetic disk and the diamond, therefore producing the largest values of g . However, the coherence time for an NV center spin decreases sharply as it approaches the surface due to magnetic noise from uncontrolled surface spins.^{36–39} Recent work has shown that the spin coherence time saturates to the bulk value for depths of ≈ 30 nm.³⁸ For this reason, we focus on NV centers positioned a minimum of 30 nm below the surface. Figure 2(b) depicts the decay of the in-plane fringe field of the $(6, 1, 1)$ mode into the diamond substrate, showing the field at the depths of $z = -30$ nm, $z = -45$ nm and $z = -60$ nm represented by the blue, red and yellow planes, respectively. Although the fringe field decays exponentially into the diamond substrate, $|\mathbf{h}| \propto e^{k_0 z}$ [Eq. (5)], the attenuation of the field amplitude from $z = -30$ nm to $z = -60$ nm is only roughly a factor of 1/2. In the thin disk regime, $R \gg d$, $|\mathbf{h}|$ decays with a scale $\approx R$ and not $\approx d$, as $e^{k_0 z} \approx 1 + z/R$. The enhancement and localization of the fringe field amplitude for larger angular modes m can also be visualized in Fig. 2(c), where the fringe fields are shown in a cross section plane $\theta = 0$ [blue plane in Fig. 2(c)] for the modes $(4, 1, 1)$, $(5, 1, 1)$ and $(6, 1, 1)$.

Spin-magnon coupling — Here we investigate the coupling between magnon modes and NV center spins. In the presence of external magnetic field \mathbf{B}_{ex} , the ground state spin 1 Hamiltonian for an NV center, written in the $|m_s\rangle$ basis along the NV axis, $| -1 \rangle, | 0 \rangle, | +1 \rangle$

²The fringe fields of higher modes possess nodes along the vertical (z) and radial (r) directions, which in turn diminish the amplitude of the fringe fields.

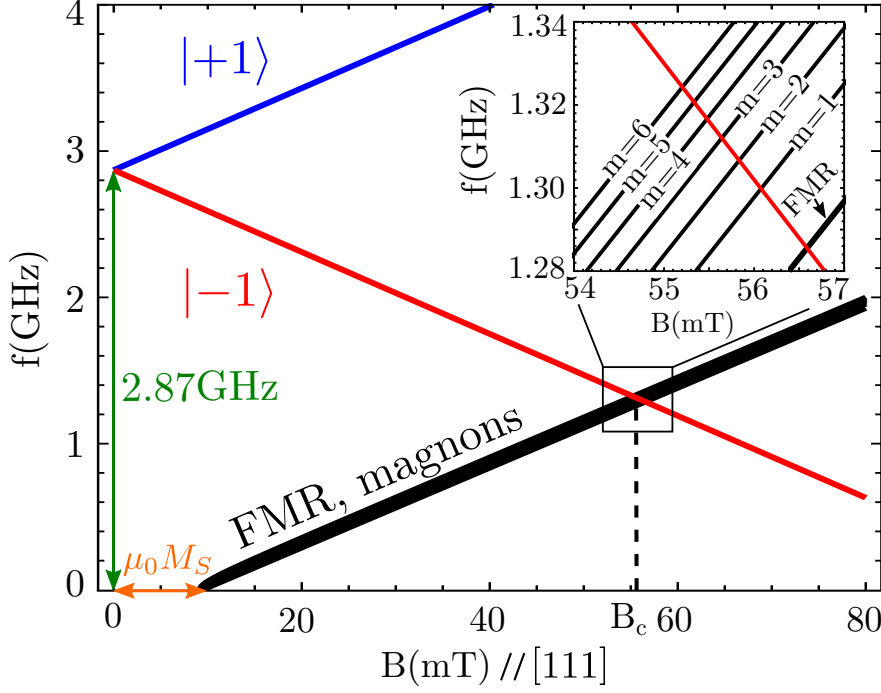


Figure 3: Frequencies of NV center levels $|\pm 1\rangle$ (blue and red solid lines), FMR and magnons (black solid lines) as a function of external dc magnetic field B parallel to the [111] Diamond crystallographic direction and NV center axis. Inset shows a zoom-in of the crossing region between $|-1\rangle$ level with both magnonic $m = 1, 2, 3, 4, 5, 6$ and FMR frequencies.

is^{3,4,7,40–54,54,55,55–61}

$$\frac{\mathcal{H}_{NV}}{2\pi\hbar} = D \left(S_z^2 - \frac{2}{3} \right) + \frac{\mu_B}{2\pi\hbar} \mathbf{B}_{ex} \cdot \bar{g} \cdot \mathbf{S} \quad (6)$$

where \bar{g} is the g-factor tensor, \mathbf{S} is represented by the spin-1 matrices, \hbar is the reduced Planck constant and $D = 2.87$ GHz is the zero-field splitting between $|0\rangle$ and the degenerate states at zero field $|\pm 1\rangle$.

In Fig. 3 we plot the resonant frequencies of the uniform FMR mode, magnon modes, [Eq. (4)] and the NV center spin [Eq. (6)] as a function of B_{dc} oriented along the [111] symmetry axis of the NV center (Fig. 1). The frequency corresponding to the $|0\rangle \rightarrow |-1\rangle$ transition crosses both the FMR and magnon frequencies at $B_c \approx 56$ mT and $f \approx 1.30$ GHz. Due to the low saturation magnetization of $\text{V}[\text{TCNE}]_x$, the different angular mode frequencies associated to the magnon modes $m = 1, 2, 4, 5, 6$ are not resolved within the scale of Fig. 3.

The inset of Fig. 3 provides enough resolution to see that the different angular modes $m = 1, 2, 3, 4, 5, 6$ and the FMR can now be distinguished.

The spin-magnon coupling is described by a Jaynes-Cumming Hamiltonian,⁶² in which the coupling originates from the Zeeman Hamiltonian $g\mu_B\mathbf{B}_{ex} \cdot \mathbf{S}$. The total magnetic field is a sum of the dc applied external magnetic field \mathbf{B}_{dc} and the magnon rf fringe fields $\mathbf{h}_\lambda(\mathbf{r}, t)$ [Eq. (5)]. After applying the rotating wave approximation (RWA), and under resonant conditions, the NV center-magnon coupling Hamiltonian

$$\frac{\mathcal{H}_I}{2\pi\hbar} = g_\lambda(\mathbf{r}_{NV})a_\lambda^\dagger S_+ + g_\lambda^*(\mathbf{r}_{NV})a_\lambda S_-, \quad (7)$$

with coupling between the NV center spin and the λ magnon mode

$$g_\lambda(\mathbf{r}_{NV}) = \frac{g\mu_B\mu_0}{8\pi\hbar} \bar{h}_{-, \lambda}(\mathbf{r}_{NV}) \quad (8)$$

for a NV center located at $\mathbf{r} = \mathbf{r}_{NV}$. Here we write Eq. 8 to preserve the position-dependent phase of g_λ to account for the possibility of coupling two NV spins to the same magnon mode. In Eq. (7) the term $a_\lambda S_+$ ($a_\lambda^\dagger S_-$) corresponds to the raising (lowering) of the NV center spin, combined with a creation (annihilation) of a magnon (since the $| -1 \rangle$ state has higher energy than the $| 0 \rangle$ spin state). For the magnon mode $\lambda = (6, 1, 1)$ at 30 nm below the bottom disk surface ($z = -45$ nm), we find $|\bar{h}_{-, \lambda}| \approx 0.65$ A/m [See Fig. 2(b)], which yields $g_{(6,1,1)} = 8.7$ kHz.

The cooperativity,

$$\mathcal{C}_\lambda = \frac{4\bar{g}_\lambda^2}{n\kappa/T_2^*}, \quad (9)$$

characterizes how often the magnon-spin system can coherently swap quantum information between magnon occupancy and the spin state. Here $\bar{g}_\lambda = |g_\lambda(\mathbf{r}_{NV})|\sqrt{2}$, T_2^* is the free precession coherence time of NV center, κ is the magnon damping rate and $n = 1/(e^{\hbar\omega_\lambda/k_B T} - 1)$ the average thermal number of magnons, where k_B is the Boltzmann constant. We as-

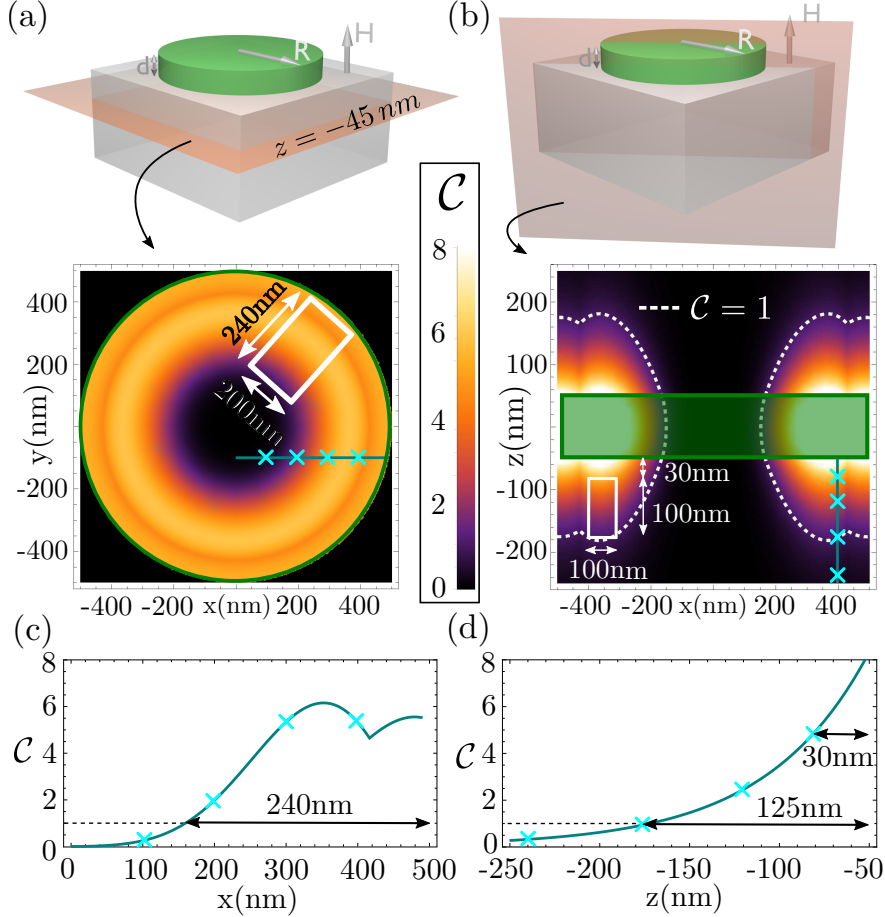


Figure 4: Spatial-plot of the cooperativity of the $\lambda = (6, 1, 1)$ magnon mode (a) at 30 nm below the disk ($z = -45$ nm), (b) within cross-section plane, (c) along the teal line within Fig. 4(a), (d) along the teal line within Fig. 4(b). The dashed white border shows the strong-regime stability region where $\mathcal{C}_\lambda \geq 1$, where the white rectangle indicates a tolerance for spatial implantation imprecision for the NV centers while still achieving high cooperativity. The green lines delimit the disk dimension $d = 100$ nm and $R = 500$ nm.

sume³⁴ $T_2^* \approx 1.5 \times 10^{-3}$ s and note that for $T \lesssim 100$ mK, $n \approx 1$. The magnon damping rate $\varkappa = 100$ kHz is obtained from the homogeneous ferromagnetic resonance linewidth, $\varkappa = f/Q$, where⁶³ $Q = 1/(2\alpha)$ with³² $\alpha = 4 \times 10^{-5}$ and $f \approx 1.3$ GHz for V[TCNE]_x.³ As an upper bound, $\varkappa \sim 300$ kHz from the inhomogeneous broadening linewidth, for which³² $Q = 3700$

We find that the cooperativity $\mathcal{C} > 1$ for a wide range of positions of the NV spin near the disk, as shown in Fig. 4 for the (6, 1, 1) magnon mode. Figure 4(a) shows \mathcal{C} for the plane

³Here we use the V[TCNE]_x damping α measured at room temperature.

positioned 30 nm below the disk ($z = -45$ nm), whereas Fig. 4(b) shows \mathcal{C} as a function of the NV depth in a cross-sectional plane. $\mathcal{C} > 1$ within those regions surrounded by white dashed lines in Fig. 4(b). We focus on the regions delineated by solid white lines, whose dimensions are ≥ 100 nm, because the spatial precision of implanting NV spins is ≈ 20 nm, due to straggle and finite aperture size.^{64,65} Figs. 4(c) and (d) show the variation of the cooperativity along the teal lines in Figs. 4(a) and (b), respectively. Therefore, two NV centers that in principle could be directly coupled only if separated by $\lesssim 20$ nm, could now be coupled through a magnon mode when separated by $\approx 2R \approx 1 \mu\text{m}$.

The cooperativity, Eq. (9), is the product of a geometric factor $\Gamma_\lambda(R, d, \mathbf{r})$ (dimension and position dependent), a material factor M_S/α (material dependent) and the reciprocal magnon energy $\hbar\omega_\lambda$

$$\mathcal{C}_\lambda = \gamma T_2^* \frac{(g\mu_B\mu_0)^2}{4\pi n} \Gamma_\lambda(R, d, \mathbf{r}_{\text{NV}}) \times \frac{1}{\hbar\omega_\lambda} \times \frac{M_s}{\alpha}. \quad (10)$$

The linear dependence on M_S comes from the amplitude of the fringe fields. This equation provides an analytical formula for the cooperativity of any magnetic disk on top of a diamond substrate, and thus it, along with estimates for the quantities therein, are significant theoretical results of our work. Using this formula, we can analytically compare the cooperativity for the same material with different disk dimensions, and for different materials in the same geometry. For instance, we evaluate the cooperativity for the same magnon mode (6, 1, 1) for a disk with double the diameter ($R = 1 \mu\text{m}$). We obtain through Eq. (10) that $C_{(6,1,1)}^{1\mu\text{m}} \approx 2.5$ for a NV center spin located 30 nm below the V[TCNE]_x bottom surface; in general, disks with smaller diameter than $3.8\mu\text{m}$ will permit $C_{(6,1,1)} > 1$ for this magnon mode and NV depth.

Comparison with YIG.— For out-of-plane magnetization there is no resonance between the above magnon mode in a YIG disk and NV center levels, considering low-temperature thin film values^{22,23,66} of M_S (≈ 2200 G) (see Supplemental Material³⁵). The shift by $\mu_0 M_S$

of both magnon and FMR frequencies along the B axis [coming from $f \approx \gamma(B/\mu_0 - M_S)$] moves the magnonic and FMR dispersions away from the NV level (see orange arrow within Fig. 3). A resonance condition occurs for $M_S \lesssim 1800$ or for much higher index magnon modes. Furthermore, at low temperature the damping for thin-film YIG increases by a factor of $\approx 6 - 30$, reaching $\approx 1.5 \times 10^{-3}$ in Ref.²² and $\approx 18 \times 10^{-3}$ in Ref.²³ — possibly due to the impurity relaxation from rare earth or Fe^{2+} ions.^{67–72} Using now Eq. (10) we compare the cooperativity between YIG and $\text{V}[\text{TCNE}]_x$ for the same $(6, 1, 1)$ magnon mode assuming M_S^{YIG} has been somehow reduced to 1750 G. We obtain $\mathcal{C}_{\text{YIG}} < 1$ for the smallest thin-film²² α and $\mathcal{C}_{\text{YIG}} \approx 30 \approx 5\mathcal{C}_{\text{V}[\text{TCNE}]_x}$ for the $\alpha \approx 5 \times 10^{-5}$ observed⁷³ in low-temperature bulk YIG (see Supplemental Material³⁵). Therefore, we conclude that despite the large M_S of YIG (which enhances \mathcal{C} through an enhanced rf fringe field), the large observed thin-film damping values at low-temperature currently make YIG a less favorable material than $\text{V}[\text{TCNE}]_x$ for realizing the strong coupling regime. However, if thin-film YIG damping values could be brought towards the bulk value $\alpha_{\text{YIG,bulk}}$,⁷³ and the resonance frequency mismatch fixed (*e.g.* by reducing M_s by about 25%), the cooperativity could exceed that of $\text{V}[\text{TCNE}]_x$ in the desired geometry (1 μm diameter disk directly on diamond).

Experimental challenges. — The experimental realization of this device structure presents a series of challenges that can be grouped into four broad categories: i) the ability to create $\text{V}[\text{TCNE}]_x$ discs on a diamond surface without loss of magnon coherence, ii) the creation of near-surface NV centers with long spin lifetime, iii) measurement at milli-Kelvin temperatures, and iv) developing approaches to gate the interaction, thus enabling controlled entanglement. We briefly consider those challenges here.

Recent work has demonstrated that $\text{V}[\text{TCNE}]_x$ can be patterned down to micron length scales on arbitrary substrates while maintaining damping values consistent with the thin-film values quoted here³² ($\alpha = 4 \times 10^{-5}$). Prior results have shown that various packaging strategies allow for measurement under ambient conditions⁷⁴ and down to cryogenic temperatures.⁷⁵ Fluctuations of paramagnetic spins at the diamond surface have been shown

to contribute to NV spin dephasing, and so in a real device some compromise must be made between shallow positioning for increased coupling to magnons and deeper positioning for longer spin coherence times. Combining our calculations with recent experimental measurements of NV spin lifetime³⁸ suggest that a depth of roughly 30 nm will provide the optimal cooperativity. Finally, measuring at temperatures below 100 mK presents experimental challenges, however, they have been solved previously for both microwave and optical measurements.⁷³ The damping of $V[TCNE]_x$ magnons at these temperatures has not been studied, however we note that in studies of YIG under similar conditions the *intrinsic* magnon damping decreases with decreasing temperature. In YIG, this decrease is swamped by a dramatic increase in *extrinsic* damping due to fluctuations of paramagnetic defects in the GGG substrate and in the YIG film itself.⁶⁷⁻⁷² We anticipate that the ability to deposit $V[TCNE]_x$ directly onto the diamond surface will substantially mitigate these effects and may allow us to exploit the intrinsic decrease in damping. Finally it will be important to shift the bias magnetic field on microsecond timescales to bring the NV center spin(s) in and out of resonance with the magnon modes. This can be achieved with Oersted fields generated by passing currents through lithographically defined wires on the diamond surface, a geometry previously realized for [111]-oriented NV centers.³³

Concluding remarks.— The spin-magnon coupling predicted here is suitable for entanglement and transduction among NV spins and single magnon occupancy of a magnon mode. Through an analytical calculation we find that for high angular index magnon modes of a $1\ \mu\text{m}$ $V[TCNE]_x$ disk, the spin-magnon coupling strength $g \approx 10$ kHz. We also predict a cooperativity of $\mathcal{C} \approx 6$ within a wide spatial area within the diamond substrate, sufficiently far below the surface to avoid uncontrolled surface spin noise, thus making our proposal experimentally realizable and not sensitively dependent on the NV center position. We also calculate \mathcal{C} for YIG instead of $V[TCNE]_x$, and we find smaller cooperativities in the case of thin-film YIG, due to the larger demagnetization field and the higher low-temperature, patterned thin-film damping. The geometry and materials we propose here provide a practical

approach for strongly coupling NV centers that are separated by $\approx 1 \mu\text{m}$, providing possible avenues to assist quantum networking.

Acknowledgement

The material is based on work supported by the U.S. Department of Energy, Office of Basic Energy Sciences, under Award Number DE-SC0019250. We would like to acknowledge D. D. Awschalom, M. Chilcote, A. R. da Cruz, K. Hu, S. R. McMillan, and C. Şahin for useful and valuable discussions.

References

- (1) Degen, C. L.; Reinhard, F.; Cappellaro, P. Quantum sensing. *Rev. Mod. Phys.* **2017**, *89*, 035002.
- (2) Zhou, B. B.; Jerger, P. C.; Lee, K.-H.; Fukami, M.; Mujid, F.; Park, J.; Awschalom, D. D. Spatiotemporal Mapping of a Photocurrent Vortex in Monolayer MoS₂ Using Diamond Quantum Sensors. *Phys. Rev. X* **2020**, *10*, 011003.
- (3) others,, et al. Quantum entanglement between an optical photon and a solid-state spin qubit. *Nature* **2010**, *466*, 730.
- (4) de Lange, G.; Wang, Z. H.; Ristè, D.; Dobrovitski, V. V.; Hanson, R. Universal Dynamical Decoupling of a Single Solid-State Spin from a Spin Bath. *Science* **2010**, *330*, 60–63.
- (5) others,, et al. Loophole-free Bell inequality violation using electron spins separated by 1.3 kilometres. *Nature* **2015**, *526*, 682–686.
- (6) Dobrovitski, V.; Fuchs, G.; Falk, A.; Santori, C.; Awschalom, D. Quantum Control over Single Spins in Diamond. *Annual Review of Condensed Matter Physics* **2013**, *4*, 23–50.

(7) Doherty, M. W.; Manson, N. B.; Delaney, P.; Jelezko, F.; Wrachtrup, J.; Hollenberg, L. C. The nitrogen-vacancy colour centre in diamond. *Physics Reports* **2013**, *528*, 1 – 45.

(8) Casola, F.; van der Sar, T.; Yacoby, A. Probing condensed matter physics with magnetometry based on nitrogen-vacancy centres in diamond. *Nature Reviews Materials* **2018**, *3*, 1–13.

(9) Awschalom, D. D.; Hanson, R.; Wrachtrup, J.; Zhou, B. B. Quantum technologies with optically interfaced solid-state spins. *Nature Photonics* **2018**, *12*, 516–527.

(10) Wehner, S.; Elkouss, D.; Hanson, R. Quantum internet: A vision for the road ahead. *Science* **2018**, *362*.

(11) others,, et al. Quantum register based on coupled electron spins in a room-temperature solid. *Nature Physics* **2010**, *6*, 249–253.

(12) Dolde, F.; Jakobi, I.; Naydenov, B.; Zhao, N.; Pezzagna, S.; Trautmann, C.; Meijer, J.; Neumann, P.; Jelezko, F.; Wrachtrup, J. Room-temperature entanglement between single defect spins in diamond. *Nature Physics* **2013**, *9*, 139–143.

(13) Kortan, V. R.; Şahin, C.; Flatté, M. E. Nanometer-scale exchange interactions between spin centers in diamond. *Phys. Rev. B* **2016**, *93*, 220402.

(14) Trifunovic, L.; Pedrocchi, F. L.; Loss, D. Long-Distance Entanglement of Spin Qubits via Ferromagnet. *Phys. Rev. X* **2013**, *3*, 041023.

(15) Van der Sar, T.; Casola, F.; Walsworth, R.; Yacoby, A. Nanometre-scale probing of spin waves using single electron spins. *Nature communications* **2015**, *6*, 1–8.

(16) Page, M. R.; Guo, F.; Purser, C. M.; Schulze, J. G.; Nakatani, T. M.; Wolfe, C. S.; Childress, J. R.; Hammel, P. C.; Fuchs, G. D.; Bhalla, V. P. Optically detected fer-

romagnetic resonance in metallic ferromagnets via nitrogen vacancy centers in diamond. *arXiv:1607.07485* **2016**,

(17) Du, C.; van der Sar, T.; Zhou, T. X.; Upadhyaya, P.; Casola, F.; Zhang, H.; Onbasli, M. C.; Ross, C. A.; Walsworth, R. L.; Tserkovnyak, Y.; Yacoby, A. Control and local measurement of the spin chemical potential in a magnetic insulator. *Science* **2017**, *357*, 195–198.

(18) Andrich, P.; Charles, F.; Liu, X.; Bretscher, H. L.; Berman, J. R.; Heremans, F. J.; Nealey, P. F.; Awschalom, D. D. Long-range spin wave mediated control of defect qubits in nanodiamonds. *npj Quantum Information* **2017**, *3*, 1–7.

(19) Eichler, C.; Sigillito, A. J.; Lyon, S. A.; Petta, J. R. Electron Spin Resonance at the Level of 10^4 Spins Using Low Impedance Superconducting Resonators. *Phys. Rev. Lett.* **2017**, *118*, 037701.

(20) Hahn, C.; Naletov, V. V.; de Loubens, G.; Klein, O.; d'Allivy Kelly, O.; Anane, A.; Bernard, R.; Jacquet, E.; Bortolotti, P.; Cros, V.; Prieto, J. L.; Muoz, M. Measurement of the intrinsic damping constant in individual nanodisks of $\text{Y}_3\text{Fe}_5\text{O}_{12}$ and $\text{Y}_3\text{Fe}_5\text{O}_{12}|\text{Pt}$. *Applied Physics Letters* **2014**, *104*, 152410.

(21) Jungfleisch, M. B.; Zhang, W.; Jiang, W.; Chang, H.; Sklenar, J.; Wu, S. M.; Pearson, J. E.; Bhattacharya, A.; Ketterson, J. B.; Wu, M.; Hoffmann, A. Spin waves in micro-structured yttrium iron garnet nanometer-thick films. *Journal of Applied Physics* **2015**, *117*, 17D128.

(22) Haidar, M.; Ranjbar, M.; Balinsky, M.; Dumas, R. K.; Khartsev, S.; kerman, J. Thickness- and temperature-dependent magnetodynamic properties of yttrium iron garnet thin films. *Journal of Applied Physics* **2015**, *117*, 17D119.

(23) Jermain, C. L.; Aradhya, S. V.; Reynolds, N. D.; Buhrman, R. A.; Brangham, J. T.;

Page, M. R.; Hammel, P. C.; Yang, F. Y.; Ralph, D. C. Increased low-temperature damping in yttrium iron garnet thin films. *Phys. Rev. B* **2017**, *95*, 174411.

(24) Heyroth, F.; Hauser, C.; Trempler, P.; Geyer, P.; Syrowatka, F.; Dreyer, R.; Ebbinghaus, S.; Woltersdorf, G.; Schmidt, G. Monocrystalline Freestanding Three-Dimensional Yttrium-Iron-Garnet Magnon Nanoresonators. *Phys. Rev. Applied* **2019**, *12*, 054031.

(25) Pokhodnya, K.; Bonner, M.; Prigodin, V.; Epstein, A. J.; Miller, J. S. Carrier transport in the V[TCNE]_x (TCNE = tetracyanoethylene ; x ~ 2) organic-based magnet. *Journal of Physics: Condensed Matter* **2013**, *25*, 196001.

(26) Yu, H.; Harberts, M.; Adur, R.; Lu, Y.; Hammel, P. C.; Johnston-Halperin, E.; Epstein, A. J. Ultra-narrow ferromagnetic resonance in organic-based thin films grown via low temperature chemical vapor deposition. *Applied Physics Letters* **2014**, *105*, 012407.

(27) Cimpoesu, F.; Frecus, B.; Oprea, C. I.; Panait, P.; Gru, M. A. Disorder, exchange and magnetic anisotropy in the room-temperature molecular magnet V[TCNE]_x A theoretical study. *Computational Materials Science* **2014**, *91*, 320 – 328.

(28) Harberts, M.; Lu, Y.; Yu, H.; Epstein, A. J.; Johnston-Halperin, E. Chemical vapor deposition of an organic magnet, vanadium tetracyanoethylene. *JoVE (Journal of Visualized Experiments)* **2015**, e52891.

(29) Zhu, N.; Zhang, X.; Froning, I. H.; Flatt, M. E.; Johnston-Halperin, E.; Tang, H. X. Low loss spin wave resonances in organic-based ferrimagnet vanadium tetracyanoethylene thin films. *Applied Physics Letters* **2016**, *109*, 082402.

(30) others,, et al. Organic-based magnon spintronics. *Nature materials* **2018**, *17*, 308–312.

(31) Chilcote, M.; Harberts, M.; Fuhrmann, B.; Lehmann, K.; Lu, Y.; Franson, A.; Yu, H.; Zhu, N.; Tang, H.; Schmidt, G.; Johnston-Halperin, E. Spin-wave confinement and coupling in organic-based magnetic nanostructures. *APL Materials* **2019**, *7*, 111108.

(32) Franson, A.; Zhu, N.; Kurfman, S.; Chilcote, M.; Candido, D. R.; Buchanan, K. S.; Flatt, M. E.; Tang, H. X.; Johnston-Halperin, E. Low-damping ferromagnetic resonance in electron-beam patterned, high-Q vanadium tetracyanoethylene magnon cavities. *APL Materials* **2019**, *7*, 121113.

(33) Fuchs, G. D.; Burkard, G.; Klimov, P. V.; Awschalom, D. D. A quantum memory intrinsic to single nitrogenvacancy centres in diamond. *Nature Physics* **2011**, *7*, 789–793.

(34) others,, et al. Ultra-long coherence times amongst room-temperature solid-state spins. *Nature communications* **2019**, *10*, 1–6.

(35) See Supplemental Material for ...

(36) Meriles, C. A.; Jiang, L.; Goldstein, G.; Hodges, J. S.; Maze, J.; Lukin, M. D.; Capellaro, P. Imaging mesoscopic nuclear spin noise with a diamond magnetometer. *The Journal of Chemical Physics* **2010**, *133*, 124105.

(37) Rosskopf, T.; Dussaux, A.; Ohashi, K.; Loretz, M.; Schirhagl, R.; Watanabe, H.; Shikata, S.; Itoh, K. M.; Degen, C. L. Investigation of Surface Magnetic Noise by Shallow Spins in Diamond. *Phys. Rev. Lett.* **2014**, *112*, 147602.

(38) Myers, B. A.; Das, A.; Dartailh, M. C.; Ohno, K.; Awschalom, D. D.; Bleszynski Jayich, A. C. Probing Surface Noise with Depth-Calibrated Spins in Diamond. *Phys. Rev. Lett.* **2014**, *113*, 027602.

(39) Sangtawesin, S. et al. Origins of Diamond Surface Noise Probed by Correlating Single-Spin Measurements with Surface Spectroscopy. *Phys. Rev. X* **2019**, *9*, 031052.

(40) Loubser, J. H. N.; van Wyk, J. A. Electron spin resonance in the study of diamond. *Reports on Progress in Physics* **1978**, *41*, 1201–1248.

(41) Oort, E. V.; Glasbeek, M. Electric-field-induced modulation of spin echoes of N – V centers in diamond. *Chemical Physics Letters* **1990**, *168*, 529 – 532.

(42) Tamarat, P.; Gaebel, T.; Rabeau, J. R.; Khan, M.; Greentree, A. D.; Wilson, H.; Hollenberg, L. C. L.; Prawer, S.; Hemmer, P.; Jelezko, F.; Wrachtrup, J. Stark Shift Control of Single Optical Centers in Diamond. *Phys. Rev. Lett.* **2006**, *97*, 083002.

(43) Hossain, F. M.; Doherty, M. W.; Wilson, H. F.; Hollenberg, L. C. L. Ab Initio Electronic and Optical Properties of the $N - V^-$ Center in Diamond. *Phys. Rev. Lett.* **2008**, *101*, 226403.

(44) Bassett, L. C.; Heremans, F. J.; Yale, C. G.; Buckley, B. B.; Awschalom, D. D. Electrical Tuning of Single Nitrogen-Vacancy Center Optical Transitions Enhanced by Photoinduced Fields. *Phys. Rev. Lett.* **2011**, *107*, 266403.

(45) Maze, J. R.; Gali, A.; Togan, E.; Chu, Y.; Trifonov, A.; Kaxiras, E.; Lukin, M. D. Properties of nitrogen-vacancy centers in diamond: the group theoretic approach. *New Journal of Physics* **2011**, *13*, 025025.

(46) others,, et al. Electric-field sensing using single diamond spins. *Nature Physics* **2011**, *7*, 459.

(47) Doherty, M. W.; Manson, N. B.; Delaney, P.; Hollenberg, L. C. L. The negatively charged nitrogen-vacancy centre in diamond: the electronic solution. *New Journal of Physics* **2011**, *13*, 025019.

(48) Acosta, V. M.; Santori, C.; Faraon, A.; Huang, Z.; Fu, K.-M. C.; Stacey, A.; Simpson, D. A.; Ganesan, K.; Tomljenovic-Hanic, S.; Greentree, A. D.; Prawer, S.; Beausoleil, R. G. Dynamic Stabilization of the Optical Resonances of Single Nitrogen-Vacancy Centers in Diamond. *Phys. Rev. Lett.* **2012**, *108*, 206401.

(49) Doherty, M. W.; Dolde, F.; Fedder, H.; Jelezko, F.; Wrachtrup, J.; Manson, N. B.; Hollenberg, L. C. L. Theory of the ground-state spin of the NV⁻ center in diamond. *Phys. Rev. B* **2012**, *85*, 205203.

(50) Dolde, F.; Doherty, M. W.; Michl, J.; Jakobi, I.; Naydenov, B.; Pezzagna, S.; Meijer, J.; Neumann, P.; Jelezko, F.; Manson, N. B.; Wrachtrup, J. Nanoscale Detection of a Single Fundamental Charge in Ambient Conditions Using the NV⁻ Center in Diamond. *Phys. Rev. Lett.* **2014**, *112*, 097603.

(51) Schirhagl, R.; Chang, K.; Loretz, M.; Degen, C. L. Nitrogen-vacancy centers in diamond: nanoscale sensors for physics and biology. *Annual review of physical chemistry* **2014**, *65*, 83–105.

(52) Dolde, F.; Doherty, M. W.; Michl, J.; Jakobi, I.; Naydenov, B.; Pezzagna, S.; Meijer, J.; Neumann, P.; Jelezko, F.; Manson, N. B.; Wrachtrup, J. Nanoscale Detection of a Single Fundamental Charge in Ambient Conditions Using the NV⁻ Center in Diamond. *Phys. Rev. Lett.* **2014**, *112*, 097603.

(53) Rogers, L. J.; Doherty, M. W.; Barson, M. S. J.; Onoda, S.; Ohshima, T.; Manson, N. B. Singlet levels of the NV-centre in diamond. *New Journal of Physics* **2015**, *17*, 013048.

(54) Ivády, V.; Szász, K.; Falk, A. L.; Klimov, P. V.; Christle, D. J.; Janzén, E.; Abrikosov, I. A.; Awschalom, D. D.; Gali, A. Theoretical model of dynamic spin polarization of nuclei coupled to paramagnetic point defects in diamond and silicon carbide. *Phys. Rev. B* **2015**, *92*, 115206.

(55) Seo, H.; Falk, A. L.; Klimov, P. V.; Miao, K. C.; Galli, G.; Awschalom, D. D. Quantum decoherence dynamics of divacancy spins in silicon carbide. *Nature communications* **2016**, *7*, 12935.

(56) Lowther, J. E. Vacancies and divacancies in cubic silicon carbide. *Journal of Physics C: Solid State Physics* **1977**, *10*, 2501–2509.

(57) Klimov, P. V.; Falk, A. L.; Buckley, B. B.; Awschalom, D. D. Electrically Driven Spin Resonance in Silicon Carbide Color Centers. *Phys. Rev. Lett.* **2014**, *112*, 087601.

(58) de las Casas, C. F.; Christle, D. J.; Ul Hassan, J.; Ohshima, T.; Son, N. T.; Awschalom, D. D. Stark tuning and electrical charge state control of single divacancies in silicon carbide. *Applied Physics Letters* **2017**, *111*, 262403.

(59) Christle, D. J.; Klimov, P. V.; de las Casas, C. F.; Szász, K.; Ivády, V.; Jokubavicius, V.; Ul Hassan, J.; Syväjärvi, M.; Koehl, W. F.; Ohshima, T.; Son, N. T.; Janzén, E.; Gali, A.; Awschalom, D. D. Isolated Spin Qubits in SiC with a High-Fidelity Infrared Spin-to-Photon Interface. *Phys. Rev. X* **2017**, *7*, 021046.

(60) Miao, K. C.; Bourassa, A.; Anderson, C. P.; Whiteley, S. J.; Crook, A. L.; Bayliss, S. L.; Wolfowicz, G.; Thiering, G.; Udvarhelyi, P.; Ivády, V.; Abe, H.; Ohshima, T.; Gali, Á.; Awschalom, D. D. Electrically driven optical interferometry with spins in silicon carbide. *Science Advances* **2019**, *5*.

(61) Anderson, C. P.; Bourassa, A.; Miao, K. C.; Wolfowicz, G.; Mintun, P. J.; Crook, A. L.; Abe, H.; Ul Hassan, J.; Son, N. T.; Ohshima, T.; Awschalom, D. D. Electrical and optical control of single spins integrated in scalable semiconductor devices. *Science* **2019**, *366*, 1225–1230.

(62) Jaynes, E. T.; Cummings, F. W. Comparison of quantum and semiclassical radiation theories with application to the beam maser. *Proceedings of the IEEE* **1963**, *51*, 89–109.

(63) Rossing, T. D. Resonance linewidth and anisotropy variation in thin films. *Journal of Applied Physics* **1963**, *34*, 995–995.

(64) Lee, J. C.; Bracher, D. O.; Cui, S.; Ohno, K.; McLellan, C. A.; Zhang, X.; Andrich, P.; Alemán, B.; Russell, K. J.; Magyar, A. P.; Aharonovich, I.; Bleszynski Jayich, A.; Awschalom, D.; Hu, E. L. Deterministic coupling of delta-doped nitrogen vacancy centers to a nanobeam photonic crystal cavity. *Applied Physics Letters* **2014**, *105*, 261101.

(65) McLellan, C.; Myers, B.; Kraemer, S.; Ohno, K.; Awschalom, D.; Jayich, A. B. Patterned Formation of Highly Coherent Nitrogen-Vacancy Centers Using a Focused Electron Irradiation Technique. *Nano Lett.* **2016**, *16*, 2450–2454.

(66) d'Allivy Kelly, O. et al. Inverse spin Hall effect in nanometer-thick yttrium iron garnet/Pt system. *Applied Physics Letters* **2013**, *103*, 082408.

(67) Dillon, J. F.; Nielsen, J. W. Effects of Rare Earth Impurities on Ferrimagnetic Resonance in Yttrium Iron Garnet. *Phys. Rev. Lett.* **1959**, *3*, 30–31.

(68) Spencer, E. G.; LeCraw, R. C.; Clogston, A. M. Low-Temperature Line-Width Maximum in Yttrium Iron Garnet. *Phys. Rev. Lett.* **1959**, *3*, 32–33.

(69) Rodrigue, G. P.; Meyer, H.; Jones, R. V. Resonance Measurements in Magnetic Garnets. *Journal of Applied Physics* **1960**, *31*, S376–S382.

(70) Spencer, E. G.; LeCraw, R. C.; Linares, R. C. Low-Temperature Ferromagnetic Relaxation in Yttrium Iron Garnet. *Phys. Rev.* **1961**, *123*, 1937–1938.

(71) Seiden, P. E. Ferrimagnetic Resonance Relaxation in Rare-Earth Iron Garnets. *Phys. Rev.* **1964**, *133*, A728–A736.

(72) Kittel, C. Microwave Resonance in Rare Earth Iron Garnets. *Journal of Applied Physics* **1960**, *31*, S11–S13.

(73) Tabuchi, Y.; Ishino, S.; Ishikawa, T.; Yamazaki, R.; Usami, K.; Nakamura, Y. Hybridizing Ferromagnetic Magnons and Microwave Photons in the Quantum Limit. *Phys. Rev. Lett.* **2014**, *113*, 083603.

(74) Froning, I. H.; Harberts, M.; Lu, Y.; Yu, H.; Epstein, A. J.; Johnston-Halperin, E. Thin-film encapsulation of the air-sensitive organic-based ferrimagnet vanadium tetra-cyanoethylene. *Applied Physics Letters* **2015**, *106*, 122403.

(75) Fang, L.; Bozdag, K. D.; Chen, C.-Y.; Truitt, P. A.; Epstein, A. J.; Johnston-Halperin, E. Electrical Spin Injection from an Organic-Based Ferrimagnet in a Hybrid Organic-Inorganic Heterostructure. *Phys. Rev. Lett.* **2011**, *106*, 156602.